

DRAFT VERSION JULY 27, 2022
Typeset using L^AT_EX default style in AASTeX631

And as I fixed upon the down-turned face
That pointed scrutiny with which we challenge
The first-met stranger in the waning dusk
I caught the sudden look of some dead master
Whom I had known, forgotten, half recalled
Both one and many; in the brown baked features
The eyes of a familiar compound ghost
Both intimate and unidentifiable.

T. S. Eliot
Little Gidding

Finding Peas in the Early Universe with *JWST*

JAMES E. RHOADS,¹ ISAK G. B. WOLD,^{1,2,3} SANTOSH HARISH,⁴ KEUNHO J. KIM,⁵ JOHN PHARO,⁴
SANGEETA MALHOTRA,¹ AUSTEN GABRIELPILLAI,¹ TIANXING JIANG,⁴ AND HUAN YANG⁶

¹*Astrophysics Science Division, NASA Goddard Space Flight Center, 8800 Greenbelt Road, Greenbelt, Maryland, 20771, USA*

²*Department of Physics, The Catholic University of America, Washington, DC 20064, USA*

³*Center for Research and Exploration in Space Science and Technology, NASA/GSFC, Greenbelt, MD 20771*

⁴*School of Earth and Space Exploration, Arizona State University, Tempe, AZ 85287, USA*

⁵*Department of Physics, University of Cincinnati, Cincinnati, OH 4521, USA*

⁶*Las Campanas Observatory, Carnegie Institution of Washington, Casilla 601, La Serena, Chile*

ABSTRACT

The Early Release Observations (EROs) of *JWST* beautifully demonstrate the promise of *JWST* in characterizing the universe at cosmic dawn. We analyze the ERO spectra of three $z \sim 8$ galaxies to determine their metallicities, gas temperatures and ionization. These galaxies offer the first opportunity to understand the physical properties of epoch-of-reionization galaxies through detailed rest-optical emission line spectroscopy. We show that these objects have metal abundances $12 + \log[O/H] \approx 6.9 - 8.2$, based on both the T_e method and on a recent calibration of the R_{23} metallicity indicator. Since the spectra are some of the earliest science data from *JWST*, we compare several line ratios with values expected from robust physics, to validate our measurement procedures. We compare the abundances and emission line ratios to a nearby sample of Green Pea galaxies— a population of nearby emission line galaxies whose UV properties resemble epoch-of-reionization galaxies, and which often have large Lyman continuum escape fractions. The *JWST* data show striking further similarities between these high redshift galaxies and nearby Green Peas. The $z \sim 8$ galaxies span the metallicity range covered by Green Peas. They also show the compact morphology that is typical of emission line dominated galaxies at all redshifts. Based on these similarities with Green Peas, it is likely that these are the first rest-optical spectra of galaxies that are actively driving cosmological reionization.

1. INTRODUCTION

JWST was built to visit a time when galaxies were young. In its first public release of scientific data, it has done exactly that, with rest-frame optical spectroscopy of three galaxies in the epoch of Cosmic Dawn (at redshifts $z > 7$), as well as deep imaging of a cluster field, which provides extra magnification due to gravitational lensing. In one sense,

James.E.Rhoads@nasa.gov

Sangeeta.Malhotra@nasa.gov

these are automatically young galaxies, for they are observed when the universe itself was $\lesssim 700$ Myr old, or about 5% of its current age.

There are more specific markers of youth that derive directly from the properties of individual galaxies. These include low stellar mass; active star formation; and low abundances of the heavy elements produced by nuclear fusion in stars. We will show that the most distant galaxy in the *JWST* early release NIRSpec observations is young by all of these criteria. The other two epoch-of-reionization galaxies in the same data set are still young objects by most criteria, albeit somewhat higher in both mass and metal abundance.

Detailed studies of galaxies at these redshifts will shed light on the reionization of intergalactic hydrogen, which was the landmark event of Cosmic Dawn—the first time when bound objects had a global impact on the universe. Combined constraints from the quasar spectroscopy (Fan et al. 2006; Yang et al. 2020), Ly α statistics from both line-selected (Malhotra & Rhoads 2004) and continuum-selected (Stark et al. 2010) galaxies, the cosmic microwave background (Planck Collaboration et al. 2016), and ionizing photon production models (Bouwens et al. 2015; Robertson et al. 2015; Finkelstein et al. 2019; Naidu et al. 2020) now suggest that the transition from neutral to ionized gas began before $z \approx 8.5$ and was largely finished by $z = 6.5$. Despite the expected obscuration of Ly α by neutral gas (Miralda-Escude & Rees 1998), Ly α galaxies have been identified at redshifts up to $z \approx 8.6$ (Zitrin et al. 2015), and clusters or groups of Ly α galaxies (indicating ionized bubbles) as far back as $z = 7$ (Castellano et al. 2016; Hu et al. 2021) to 7.7 (Tilvi et al. 2020). Wide area surveys for Ly α emitters at $z \approx 7$ suggest that the IGM was in fact highly ionized by $z = 7$ (Itoh et al. 2018; Zheng et al. 2017; Hu et al. 2019; Goto et al. 2021; Wold et al. 2022). Observational constraints become much poorer at higher redshifts, due largely to the difficulty of infrared observations through Earth’s atmosphere, and it is here that *JWST* is poised to drive rapid observational progress.

To place these *JWST* Cosmic Dawn galaxies in context, we have measured their rest frame optical emission line ratios. We have used the measurements to derive key physical parameters of the galaxies, notably including the gas phase oxygen abundance.

Despite the extreme properties seen in these objects, they are not without close analogs in the nearby universe. We compare the *JWST* line ratios to those of local emission line galaxy samples, including Green Pea galaxies at $z \lesssim 0.3$ (Cardamone et al. 2009; Jaskot & Oey 2013; Henry et al. 2015; Izotov et al. 2016; Yang et al. 2016, 2017; Izotov et al. 2018; Jiang et al. 2019; Brunner et al. 2020; Kim et al. 2020, 2021) and extreme emission line objects selected at $z \sim 0.6$ (Kakazu et al. 2007; Ly et al. 2016). We find that the most extreme of the *JWST* sources has a metal abundance $12 + \log[\text{O}/\text{H}] \sim 7.0$. Within present uncertainties, it may or may not be the most metal poor galaxy known. It is clear that galaxies of comparably low metallicity *do* exist in the nearby universe. But, it is equally clear that such objects are exceedingly rare at low redshift. They account for $\lesssim 1\%$ of Green Pea galaxies despite preselection using criteria, e.g. the presence of strong nebular emission lines, that should enhance their representation in that sample.

Regardless of what future data sets tell, this is a huge step forward. The first release of scientific data from *JWST* has enabled us to apply powerful tools that could previously be used only with great difficulty beyond $z \sim 1$, and even then only up to $z \sim 3$.

In this paper, we discuss the *JWST* observations (sec. 2), line ratio measurements (sec. 2.2), and consistency checks applied to the measurements (sec. 2.3); and also the selection of comparison objects from *Sloan Digital Sky Survey* Green Pea galaxies (sec. 2.4). We then present our analysis of the physical conditions drawn from the line ratio measurements (sec. 3). Finally, we discuss the implications of the results (sec. 4), and summarize our conclusions (sec. 5). Throughout the paper, where relevant, we use a flat concordance cosmology with $H_0 = 69.6 \text{ km s}^{-1} \text{ Mpc}^{-1}$, $\Omega_{tot} = 1$, $\Omega_m = 0.286$, and $\Omega_\Lambda = 0.714$.

There is a rapidly growing body of work on the *JWST* Early Release Observations, including papers that examine the properties of the same three galaxies (J072326-732656 (04590), J072322-732606 (06355), and J072320-732604 (10612)) that are our focus here. These include Carnall et al. (2022), which presents redshifts, stellar masses, and star formation histories of these galaxies; Adams et al. (2022), which recovers these three sources among a Lyman break search for $z \gtrsim 9$ objects; and Schaerer et al. (2022), which presents a metal abundance analysis with notable similarities to the present work. While most of our analysis was carried out before those works became available, we will compare our conclusions to theirs in section 4.

2. OBSERVATIONS AND DATA ANALYSIS

2.1. *JWST* observations

Table 1. Observed and derived properties of the *JWST* spectroscopic sample and of two local analogs.

ID	Spec. ID	Redshift	4363/OIII	OIII/H β	OII/H β	R23	O32	Z(R23) ^a	Te(OIII)	Z(Te) ^a
									10 ⁴ K	
J072326-732656	04590	8.495	0.058±0.014	3.92±0.33	0.30±0.11	4.18±0.38	12.26±4.25	7.2	3.72±0.99	6.88±0.15
J072322-732606	06355	7.664	0.011±0.003	9.46±0.63	1.19±0.12	10.72±0.70	7.89±0.61	8.2	1.34±0.16	8.09±0.16
J072320-732604	10612	7.659	0.029±0.011	11.92±2.06	0.71±0.28	12.67±2.23	17.29±4.49	8.2	2.19±0.54	7.68±0.24
J082701+342951	SDSS	0.0854	0.033±0.003	8.03±0.60	0.38±0.04	8.41±0.61	20.85±1.64	7.7	2.40±0.14	7.44±0.05
J122051+491555	SDSS	0.0123	0.028±0.003	4.02±0.28	0.25±0.05	4.27±0.30	16.23±3.40	7.25	2.12±0.15	7.24±0.06

^aGas phase oxygen abundances tabulated above are given in units of $12 + \log(O/H)$. Solar oxygen abundance in these units is approximately 8.7.

We used the *JWST* Early Release Observations of the galaxy cluster SMACS 0723.3-7327 (hereafter SMACS 0723), and especially the NIRSpec multi-object spectroscopy (program JW02736; observations 007 and 008). This consisted of a single configuration of the NIRSpec multi-shutter array, observed with a range of blocking filters and gratings. The most critical instrumental setup for this paper was with the F290LP blocking filter and G395M grism, which covers $\lambda_b \approx 2.9$ to $\lambda_r \approx 5.2\mu\text{m}$ with a resolving power $R \sim 1000$. The NRSIRS2 detector readout pattern was used with 20 groups, 2 integrations, and a 3 shutter slitlet nod pattern. For our targets of interest (J072326-732656 (04590), J072322-732606 (06355), J072320-732604 (10612)) this configuration resulted in on-target exposures of 8.8 ks for both observations (o007 and o008).

2.2. Emission line ratio measurements

We downloaded the Level 3 spectra for the SMACS J0723.3-7327 program from the STScI MAST server. These are pipeline calibrated products, using a mixture of ground and on-orbit calibration data (Rigby et al. 2022). We base our analysis on the 1d spectra for each of two long exposures (o007 and o008). We measured the fluxes for several detected emission lines in each spectrum, notably including [O III]4959,5007, [O III]4363, and [O II]3726,3729, and the Balmer series lines of hydrogen from H β through H ϵ .

To measure the line fluxes, we fitted Gaussian profiles to the 1D spectrum. To obtain robust fitting results on both strong and weaker lines, we performed simultaneous fits of nearby line sets, so that the wavelength and line width were effectively fixed by well detected lines, allowing more confident extraction of the weak lines. Finally, we formed line ratios separately for each of the two exposures, and combined the two line ratio estimates using an inverse variance weighting. The [O III]4959 line of J072326-732656 (04590) in the L3 exposure o008 product downloaded around July 15, 2022 appears to have some corrupted pixels, which result in a strongly negative flux measurement. We chose to replace the [O III]4959 line flux in this instance with the value expected from the theoretical [O III]4959/[O III]5007 ratio, given that the [O III]5007 line is well measured and the [O III]4959/[O III]5007 observed in exposure o007 is consistent with the theoretical value.

To estimate errors on line flux ratios, we first noted that the RMS of the continuum flux in the Level 3 1D spectra exceeded the noise reported in the L3 spectra, by a factor of ~ 1.5 to 2. We therefore applied a $2\times$ correction to the noise levels input to the line fitting software (MPFITFUN in IDL), and thereafter used the reported uncertainties in fitted line parameters to determine random line flux errors. Finally, we applied a noise floor of 5% to measured line fluxes (added in quadrature with the random flux errors reported by MPFITFUN), to allow for low level wavelength dependent calibration errors or similar systematic problems.

The line flux ratios measured through this procedure are summarized in table 1, along with derived quantities including electron temperature and gas-phase oxygen abundances (see section 3 below).

2.3. Consistency Checks and Robustness

Given that we are doing science with pipeline-processed early-release data, it is likely that there will be future refinements to the data processing and possible that these may have impact on relevant measurements. We have taken several steps to test for robustness and mitigate the impact of possible issues in data processing.

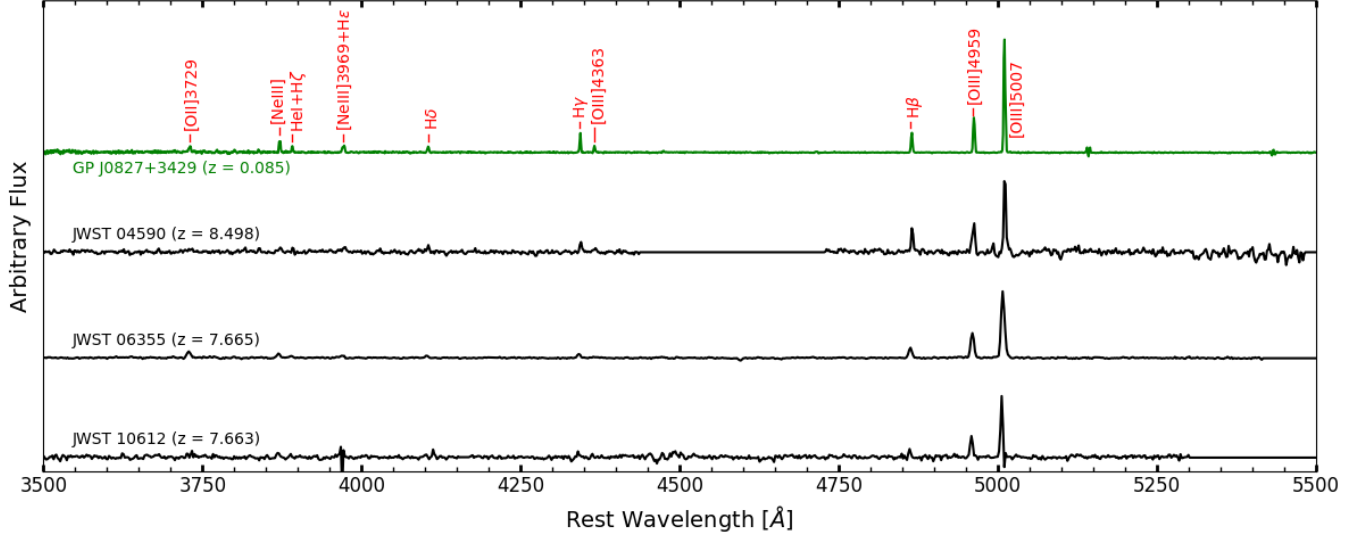


Figure 1. Comparison of the rest-optical spectra of the $z \approx 0.085$ Green Pea galaxy J0827+3429 and the epoch-of-reionization galaxies J072326-732656 (04590), J072322-732606 (06355), and J072320-732604 (10612). The Green Pea galaxy shown is selected as one of two best analogs to the line ratios of J072326-732656 (04590) among the Green Pea sample from Yang et al. (2019) and Jiang et al. (2019) (see section 2.4). For display purposes we have masked a few spurious features in these early-release JWST spectra that did not match any known spectral line, after confirming that these features were not consistently present in both exposures.

Object	exposure	4959/5007	Deviation	Hgamma/Hbeta	Deviation	Hdelta/Hbeta	Deviation
Theory	-	0.3356	0	0.474	0	0.262	0
04590	o007	0.306 ± 0.050	-0.6σ	0.679 ± 0.149	1.4σ	0.431 ± 0.155	1.1σ
04590	o008	- corrupted -	-	0.552 ± 0.101	0.7σ	0.348 ± 0.338	0.2σ
04590	combined	0.306 ± 0.050	-0.6σ	0.592 ± 0.084	1.4σ	0.417 ± 0.141	1.1σ
06355	o007	0.382 ± 0.030	1.5σ	0.523 ± 0.082	0.6σ	0.310 ± 0.318	0.2σ
06355	o008	0.371 ± 0.031	1.2σ	0.464 ± 0.077	-0.2σ	0.258 ± 0.256	0.0σ
06355	combined	0.377 ± 0.022	1.9σ	0.490 ± 0.056	0.3σ	0.278 ± 0.198	0.1σ
10612	o007	0.313 ± 0.039	-0.6σ	0.842 ± 0.391	0.9σ	0.194 ± 0.351	-0.2σ
10612	o008	0.385 ± 0.053	0.9σ	0.726 ± 0.361	0.7σ	2.04 ± 2.40	0.8σ
10612	combined	0.338 ± 0.031	0.04σ	0.779 ± 0.264	1.1σ	0.232 ± 0.230	-0.1σ

Table 2. Table of line flux ratio consistency checks. “Deviation” indicates the discrepancy between the observed and theoretical ratio, in σ units.

First, as discussed above, we renormalized the stated flux errors in the L3 spectra to bring them into line with the observed RMS continuum flux in the 1D spectra.

Second, we treated each exposure separately in measuring fluxes and forming flux ratios, and combined results statistically thereafter. This means that any overall flux normalization issue between the two exposure on each object will not impact the results. Moreover, we used only line fluxes, after subtracting a locally determined continuum level, so that our results are insensitive to any slowly varying additive component in the spectra.

We checked our measured ratios against theoretical expectations for those line ratios with values largely determined by atomic physics, namely $[\text{O III}]\lambda 4959/[\text{O III}]\lambda 5007$, where theory predicts 0.335 (Dimitrijević et al. 2007); $\text{H}\gamma/\text{H}\beta$, where theory predicts 0.474 (Osterbrock & Ferland 2006); and $\text{H}\delta/\text{H}\beta$, where theory predicts 0.262 (Osterbrock & Ferland 2006). The measured ratios are generally within $1\text{--}2\sigma$ of their theoretical values. Results of these checks are given in table 2.

Finally, we note that our key physical conclusions (section 3) depend primarily on pairs of lines that are relatively close together in wavelength. Because $[\text{O II}]\lambda 3726, 3729$ is comparatively weak in all of the objects studied here, its

impact on the inferred metallicity is modest. Therefore, the widest wavelength range that strongly affects results is the span from [O III]4363 to [O III]5007, a factor of ~ 1.15 in wavelength. This range is covered by a single NIRSpc configuration (although the two lines fall on different detectors in object J072326-732656 (04590)). The consistency checks above include the ratios $H\gamma/H\beta$ and $H\delta/H\beta$, which span a similar wavelength interval.

2.4. SDSS Green Pea comparison

The spectrum of J072326-732656 (04590) in particular is reminiscent of some of the most extreme emission line galaxies in the nearby universe. To explore this, we searched the database of Green Pea galaxies from Yang et al. (2019); Jiang et al. (2019) to find galaxies with similar line ratios. Specifically, we required $S/N([\text{O III}]\lambda 4363) > 2$, $f([\text{O III}]\lambda 4363)/f([\text{O III}]\lambda 4959,5007) > 0.035$, $f([\text{O III}]\lambda 4363)/f([\text{O II}]\lambda 3726,3729) > 0.5$, $R_{23} < 8$, and $O_{32} > 10$. This yielded two objects, J082701+342951 and J122051+491555, from a parent database of about 1000 sources (which had been previously selected on a minimum equivalent width threshold in [O III]4959,5007 and/or H β). We compare the rest-frame spectra of GP J082701+342951 and the three JWST sources in figure 1, and show both these green peas in the lower right panel of figure 2. Spectral data are taken from SDSS Data Release DR12 (Alam et al. 2015).

The similarities in most line ratios are quite striking, especially between J072326-732656 (04590) and GP J122051+491555, where all ratios apart from [O III]4363/[O III]4959,5007 are within 1σ (see table 1). This similarity gives new confidence to the conclusion that Green Peas are good analogs for epoch of reionization galaxies.

3. ANALYSIS

We measured gas-phase oxygen abundances using multiple approaches as described in the following sections.

3.1. R_{23} method

First, we apply the R_{23} metallicity method using the calibration by Jiang et al. (2019). This calibration is based on a sample of green pea galaxies, whose spectra have notable similarities to the spectrum of J072326-732656 (04590) (see figure 1). Direct interpolation off the $Z(R_{23}, O_{32})$ relation yields a metallicity estimate $12 + \log[\text{O}/\text{H}] \approx 7.2$ for J072326-732656 (04590), and 8.2 for J072322-732606 (06355) and J072320-732604 (10612) (see figure 3).

3.2. Direct method

Second, we use the well detected [OIII]4363Å line to apply the T_e (“direct”) method. Here we follow the method described in Jiang et al. (2019), which follows prior work by Izotov et al. (2006). The method uses the ratio $f([\text{O III}]\lambda 4363)/f([\text{O III}]\lambda 4959,5007)$ to measure the electron temperature in the [O III]4959,5007 emitting gas. Combining this temperature with the line flux ratio $f([\text{O III}]\lambda 4959,5007)/f(\text{H}\beta)$ furnishes an estimate of the O^{++}/H ratio. Similar methodology yields the O^+/H ratio. Figure 4 shows the relation between the observed $f([\text{O III}]\lambda 4363)/f([\text{O III}]\lambda 4959,5007)$ ratio and temperature, which is inverted numerically. The resulting value of $T_e(\text{OIII}) \approx (3.7 \pm 1) \times 10^4 \text{K}$ for J072326-732656 (04590) is extreme, though not without precedent among lower-redshift samples in the literature (e.g., Kakazu et al. 2007). The mass ratios of O^+/H and O^{++}/H are determined using fitting formulas presented by Izotov et al. (2006). The temperature of the [O II]3726,3729 emitting gas is not directly constrained, and past work has often used fitting formulas to estimate $t_2 \equiv T(\text{OII})/10^4 \text{K}$ based on $t_3 \equiv T(\text{OIII})/10^4$ (e.g., Jiang et al. (2019) uses the $T(\text{OII}) - T(\text{OIII})$ relation from Izotov et al. (2006), which is in turn based on a suite of photoionization models from Stasińska (1990)). We have used a modification of the fitting formula from Izotov et al. (2006): $t_2 = -0.577 + t_3 \times (2.065 - 0.498t_3)$ for $t_3 < 2.07$, and $t_2 = 1.562$ for $t_3 > 2.07$. This avoids an unphysical decrease of t_2 with increasing t_3 . Results (both T_e and $12 + \log[\text{O}/\text{H}]$) for all three JWST targets and the two Green Pea comparison objects are reported in table 1, and span a range $6.9 \lesssim 12 + \log[\text{O}/\text{H}] \lesssim 8.1$ that is similar to the range seen in ~ 1000 Green Peas (Jiang et al. 2019).

3.3. CLOUDY modeling for J072326-732656 (04590)

To explore the physical conditions in the most extreme of the JWST sources, J072326-732656 (04590), we have used the CLOUDY photoionization code¹ (Ferland et al. 2017) and the pyCLOUDY package (Morisset 2013) to calculate expected emission line ratios for a young, low-metallicity starburst. This package takes an input incident radiation spectrum and computes the full radiative transfer through a surrounding gas cloud, thereby predicting the resultant

¹ CLOUDY v. 17.03

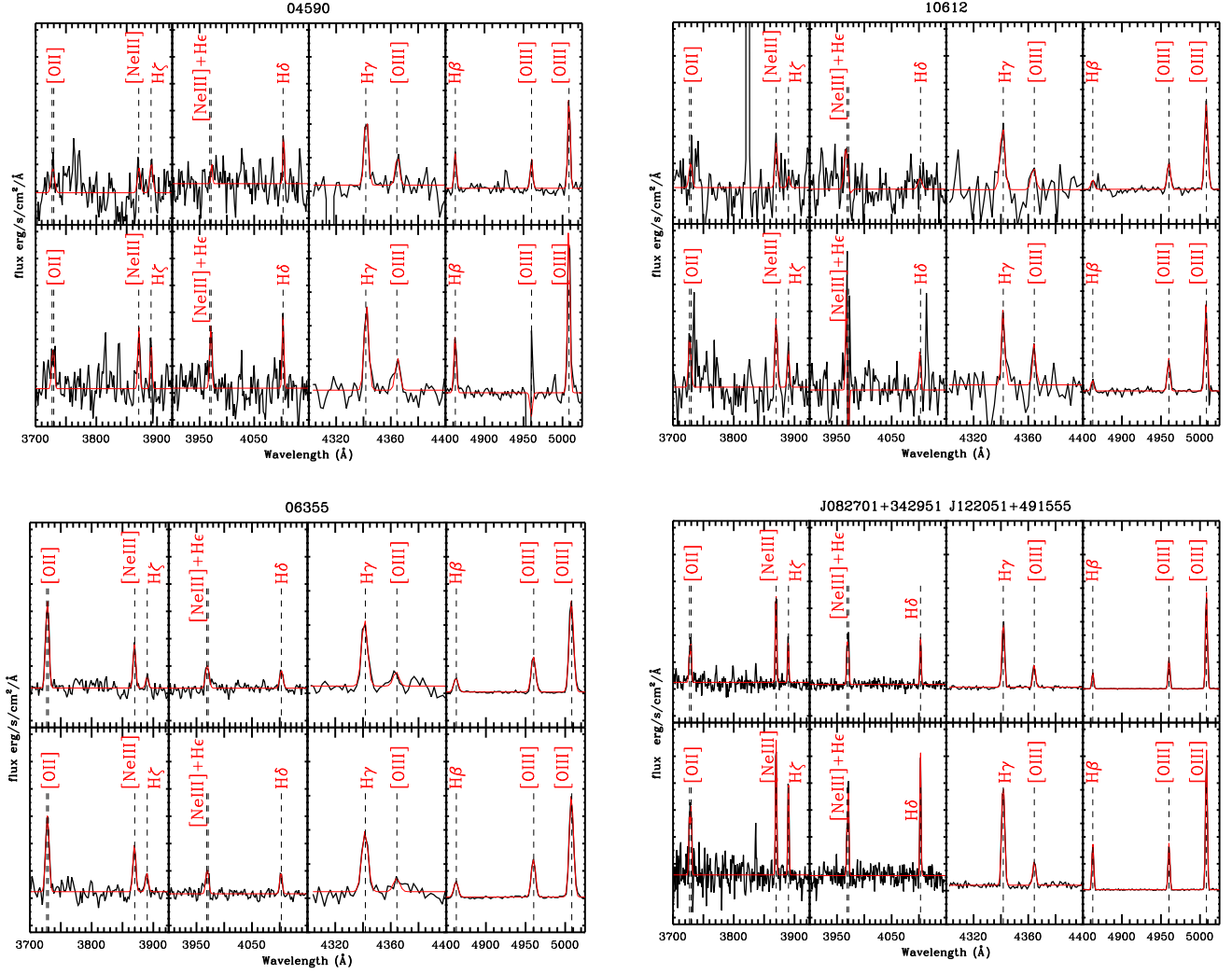


Figure 2. The emission lines and fits to these lines for objects in our analysis are shown here. The four panels correspond to J072326-732656 (04590)(top left), J072320-732604 (10612) (top right), J072322-732606 (06355) (bottom left), and two SDSS Green Pea spectra (bottom right). Within each of the JWST panels, the upper and lower rows of sub-panels correspond to the two distinct NIRSPEC exposures. For the Green Pea panel, upper and lower sub-panels correspond to two distinct objects. Within each row, four distinct wavelength segments are plotted. Each segment shows a linked line set, where we performed a joint fit to 2–4 emission lines. Each fit included three parameters to describe the redshift, line width, and continuum level, plus one parameter per emission line to measure line amplitudes. The four fitted line sets are (from blue to red) [OII] 3727, 3729 + [NeIII] 3869 + H ζ 3890; [NeIII] 3968 + H ϵ 3971 + H δ 4102; H γ 4341 + [OIII] 4364; and H β 4862 + [OIII] 4960 + [OIII] 5008.

nebular emission spectrum. We adapt the model prescriptions used in [Byler et al. \(2020\)](#), an analysis of UV and optical emission line diagnostics of metallicity and SF in young star-forming galaxies. Given the extreme observed line ratios, we adopt the minimum inner radius ($R_{inner} \sim 0.1$ pc) and maximum ionizing photon production ($Q_H \sim 10^{51} \text{ s}^{-1}$, comparable to a young star cluster) from the Byler grids, such that the model will have a high ionization parameter, U . U is also dependent on the hydrogen density n_H , and the photoionization also depends on the shape of the incident spectrum. To quickly approximate the spectrum of a young burst of low-metallicity stars, we use a blackbody spectrum with $T_{eff} = 60000$ K (comparable to CLOUDY models used in high-excitation starbursts used in e.g., [Steidel et al. 2014](#); [Sanders et al. 2016](#)).

We then run CLOUDY with these settings with grids of metallicity ($6.7 < \log(12 + O/H) < 7.5$) and electron density ($1.5 < \log(n_e) < 3$), with ranges based on estimates from the observed emission line ratios as described above (probably). As the line ratios suggest low oxygen abundances in the nebular gas, in addition to scaling the oxygen

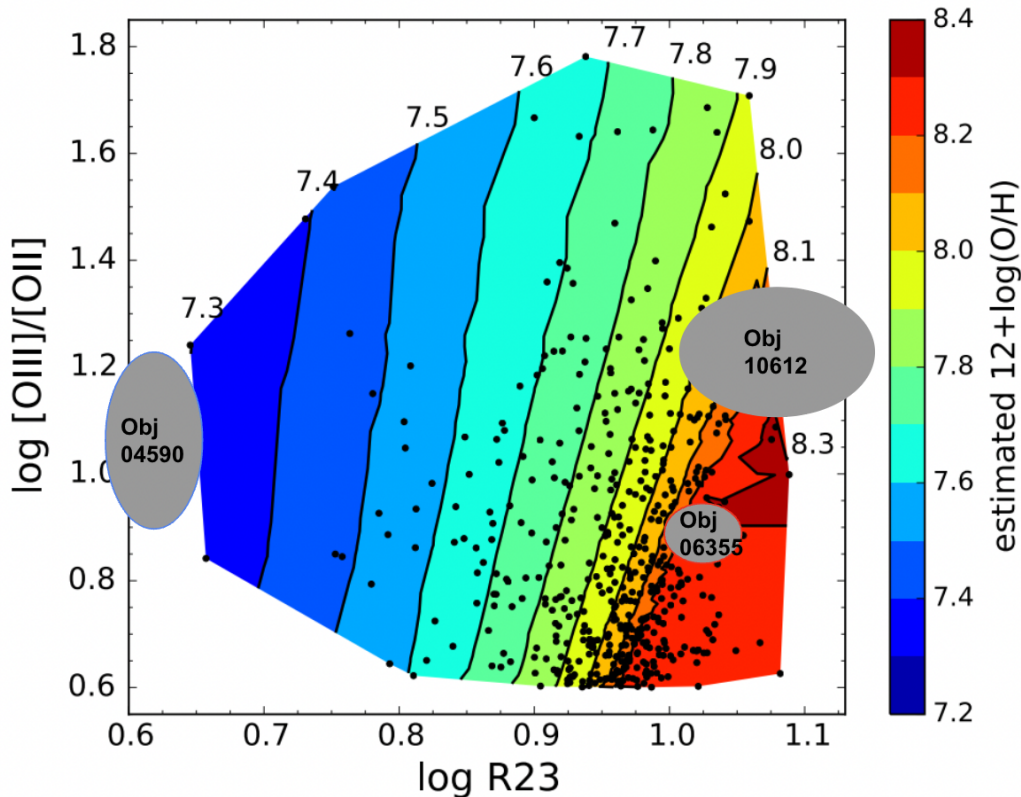


Figure 3. This figure, based on figure 8 of Jiang et al. (2019), shows the relation between R_{23} , O_{32} , and gas phase metallicity. Grey ovals mark the three $z > 7$ objects, which have inferred R_{23} metallicities of ~ 7.2 (J072326-732656 (04590)), ~ 8.2 (J072322-732606 (06355)), and ~ 8.2 (J072320-732604 (10612)). The first two measurements are in good agreement with the T_e method results, while J072320-732604 (10612) appears to be an outlier in this relation. Together, this trio of sources spans the range of R_{23} seen in the comparison sample of Green Pea galaxies.

abundance, we reduce other heavy elements in the model as well, scaling their values with the oxygen abundance. The predicted oxygen line ratios from this model grid are shown in Figure 5. Each “column” of model points represents a given density, with the left column most closely matching the density predicted from the observed OII ratio (~ 0.7 , corresponding to lower densities). The color of the points gives the gas-phase metallicity.

For the model to get close to the observed $[\text{OIII}]5007/[\text{OIII}]4363$ ratio, some combination of extremely low metallicity, high electron density, harder incident ionizing spectrum (as from e.g. particularly low stellar metallicity in the starburst), and compact cloud morphology is necessary. However, *none* of the models tested actually reproduces the $f([\text{O III}]4363)/f([\text{O III}]4959,5007)$ ratio observed in J072326-732656 (04590). We consider possible explanations in section 4 below.

3.4. Size and Surface Brightness Comparisons

Another characteristic of the local and low redshift emission line galaxies is their compact size and high star-formation rate per unit area (a.k.a, star formation surface density, Σ_{SFR}). This could be due to the dominance of one compact star-forming region (or cluster) in the galaxy. We thus examined the sizes and star-formation intensities (Star-Formation Rate per unit area Σ_{SFR}) for these galaxies. In figure 6, we show how the sizes of the three high redshift sources compare with low redshift Green Peas (Kim et al. 2021). The sizes plotted are half-light radii as derived in Source Extractor (Bertin & Arnouts 1996). The directly measured circularized half-light radii (i.e., corrected for the galaxy ellipticity) range from 0.28 to 0.42 kpc. If we apply a rough correction for lensing amplification due to the foreground galaxy cluster, using the reported magnification values from Carnall et al. (2022) which were obtained from the lens model provided by the RELICS team (Coe et al. 2019), the sizes drop to 0.1–0.26 kpc. These lensing corrections are modest for two of the sources, with the exception being an ~ 10 and a corresponding reduction in

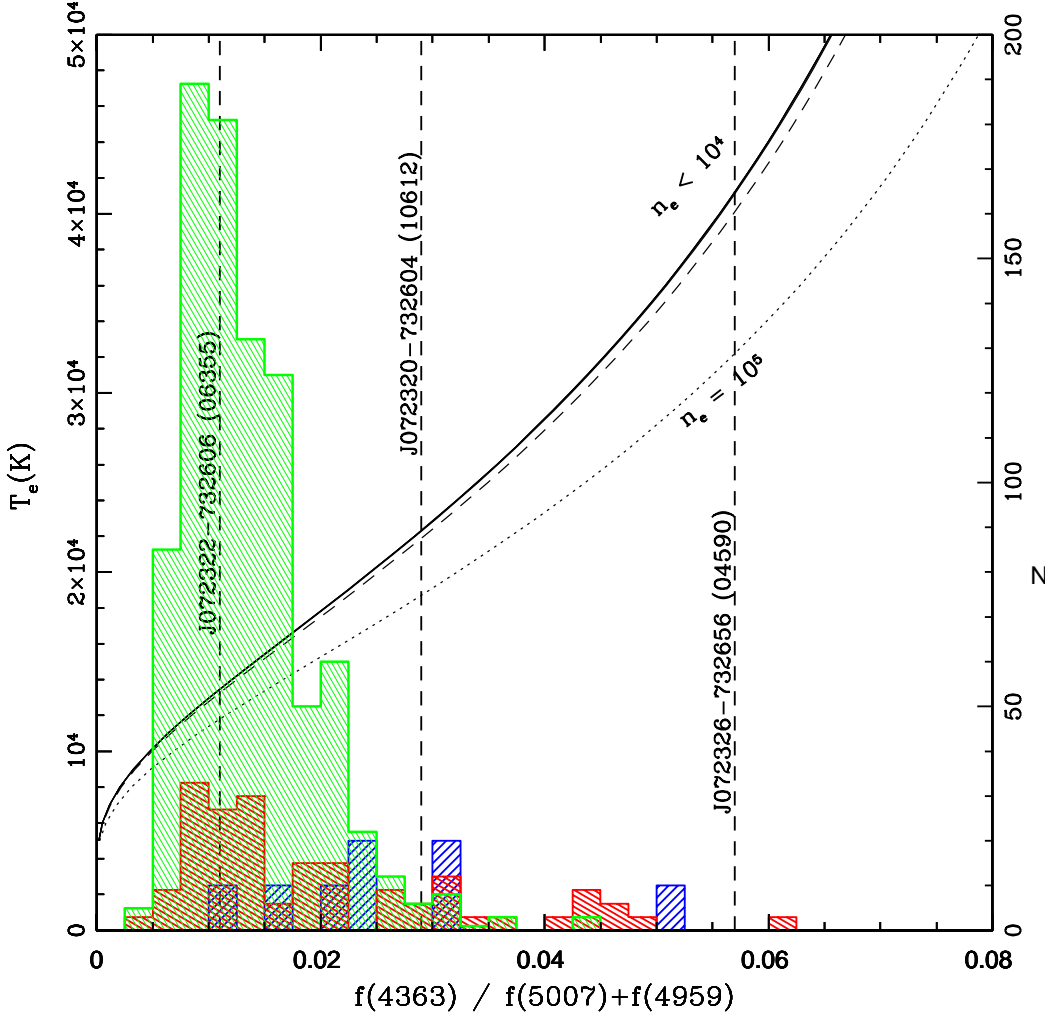


Figure 4. The electron temperature of [OIII] line emitting gas is plotted as a function of the $f(\text{OIII } 4363)/f(\text{OIII } 4959,5007)$ ratio, following the treatment in [Osterbrock & Ferland \(2006\)](#). The solid curve shows the relation in the low-density limit, approximately $n_e < 10^3 \text{ cm}^{-3}$. The dashed curve shows the relation for $n_e = 10^4 \text{ cm}^{-3}$, and the dotted curve the relation for $n_e = 10^5 \text{ cm}^{-3}$. A vertical dashed line shows the measured value of this ratio for J072326-732656 (04590). Based on this, we infer an electron temperature near 30,000K in the [OIII] region of this galaxy. Histograms of comparison samples show that the $f(\text{OIII } 4363)/f(\text{OIII } 4959,5007)$ ratio and the electron temperature in J072326-732656 (04590) are extreme but not unprecedented in lower-redshift samples. The green histogram marks the $z \lesssim 0.3$ Green Pea galaxy sample of [Yang et al. \(2019\)](#); [Jiang et al. \(2019\)](#). The blue and red histograms show intermediate redshift emission line selected samples from [Kakazu et al. \(2007\)](#) and [Ly et al. \(2016\)](#) (with numbers multiplied by 10 and 3, respectively, to display on the same y-axis as the GP sample). All comparison samples have been restricted to objects with $S/N \geq 2.5$ in the [O III]4363 line.

circularized radius of $\sim 1/3 \times$ for J072326-732656 (04590)(04590). These sizes are typical of Green Peas ($\sim 0.33 \text{ kpc}$) at low redshifts, where we have measured them from well resolved near-UV images ([Kim et al. 2021](#)).

We also calculate average star-formation intensities (SFI, equivalent to $\Sigma \text{SFR} \equiv \frac{\text{SFR}}{2\pi r_{\text{cir},50}^2} \left(\frac{\text{M}_{\odot} \text{ yr}^{-1}}{\text{kpc}^2} \right)$) for these three sources. The star-formation rate is calculated using observed rest-frame UV-continuum in F150W. We apply no dust correction. If dust corrections are in fact required, we could be under-estimating the SFI in these sources. We note that the Balmer line ratios in table 2 do not require reddening, though this is not an especially strong constraint without an $\text{H}\alpha$ measurement. To convert the measured UV luminosity to the corresponding SFR in a consistent manner with the compared Green Peas, we apply the same conversion method as in ([Kim et al. 2021](#)). we adopt the solar bolometric magnitude of 4.74 ([Bessell et al. 1998](#)), and the UV to bolometric luminosity (L_{bol}) ratio ($L_{\text{UV}}/L_{\text{bol}}$) of 0.33 and

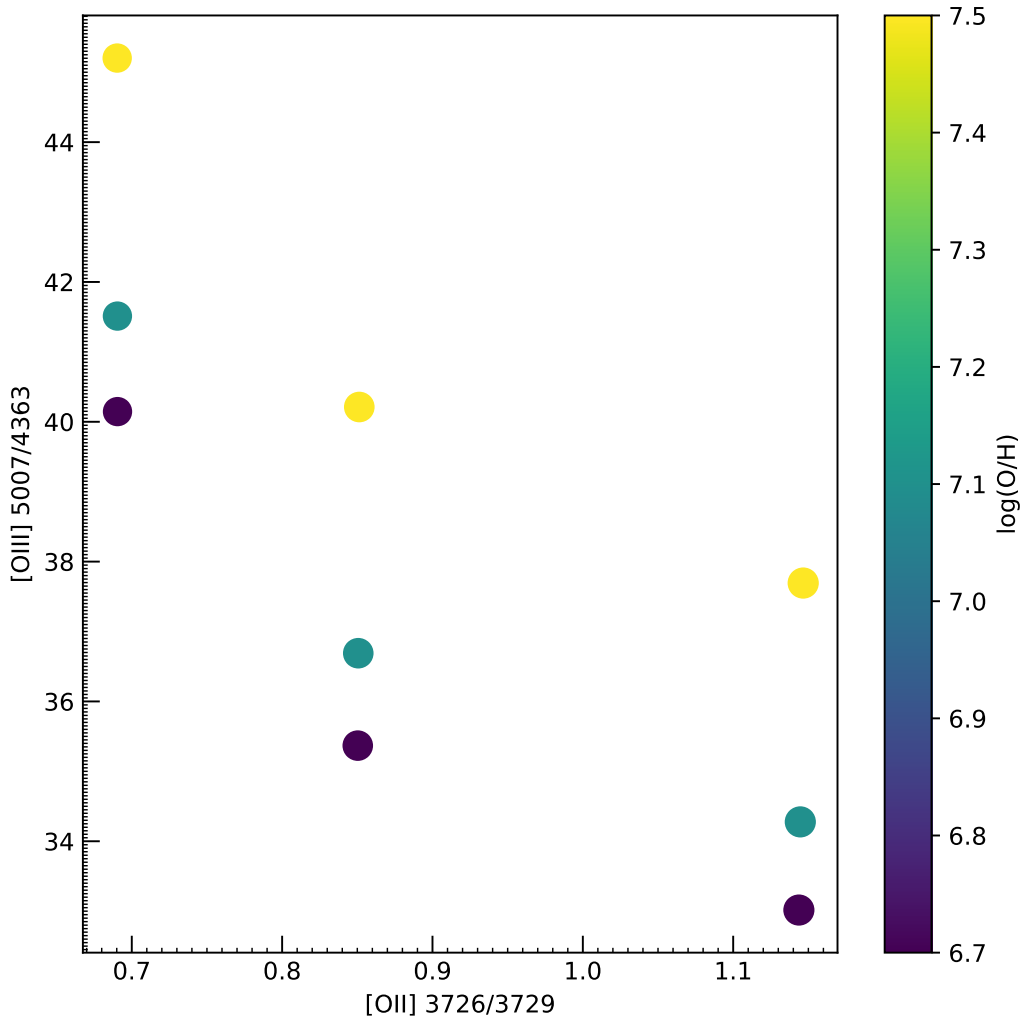


Figure 5. CLOUDY model results, showing the line ratios of [O III]4959,5007 to [O III]4363 and [O II]3726 to [O II]3729 for a grid of models with electron densities of $10^{1.5}$, $10^{2.5}$, and 10^3cm^{-3} [from left to right], and gas phase oxygen abundances $12 + \log[\text{O}/\text{H}] = 7.5, 7.1, 6.7$ [from top to bottom]. Despite examining intense and low-metallicity conditions, none of the models tested reproduce the [O III]4363/[O III]4959,5007 ratio observed in J072326-732656 (04590) (although they match the value for J072320-732604 (10612) and easily exceed that for J072322-732606 (06355), which could be matched with less extreme models). More detail on the models is presented in section 3.3, and discussion of the implications is in section 4.

the scale factor $L_{\text{bol}}/(4.5 \times 10^9 L_{\odot}) = \text{SFR}/(1M_{\odot} \text{yr}^{-1})$ that are derived from the starburst population modelling by Meurer et al. (1997). The derived SFR is then combined with size measurements to calculate the SFI. Note that the SFI is conserved by lensing, since the luminosity increases by the same factor as the area. The SFI is consistent with those of low-redshift analogs such as green peas, and is also seen to be hitting the maximum limit seen in local and high-redshift sources as shown by Meurer et al. (1997); Hathi et al. (2008).

4. DISCUSSION

The difficulties in reproducing the observed line ratios of J072326-732656 (04590) using photoionization models deserves further attention. One reasonably likely explanation is that an additional heating source may be present, driving T_e to higher values than photoionization by a starburst tends to achieve. Either photo-heating by an active galactic nucleus (AGN), or shock heating of the gas, could contribute. Either of these may have spectroscopic signatures detectable with further *JWST* observations.

A second possible class of explanation is density. The critical density for collisional de-excitation of the [O III]4363 line is much higher than for [O III]4959,5007, and for densities $n_e \gtrsim 10^5 \text{cm}^{-3}$, the observed line ratio can be achieved

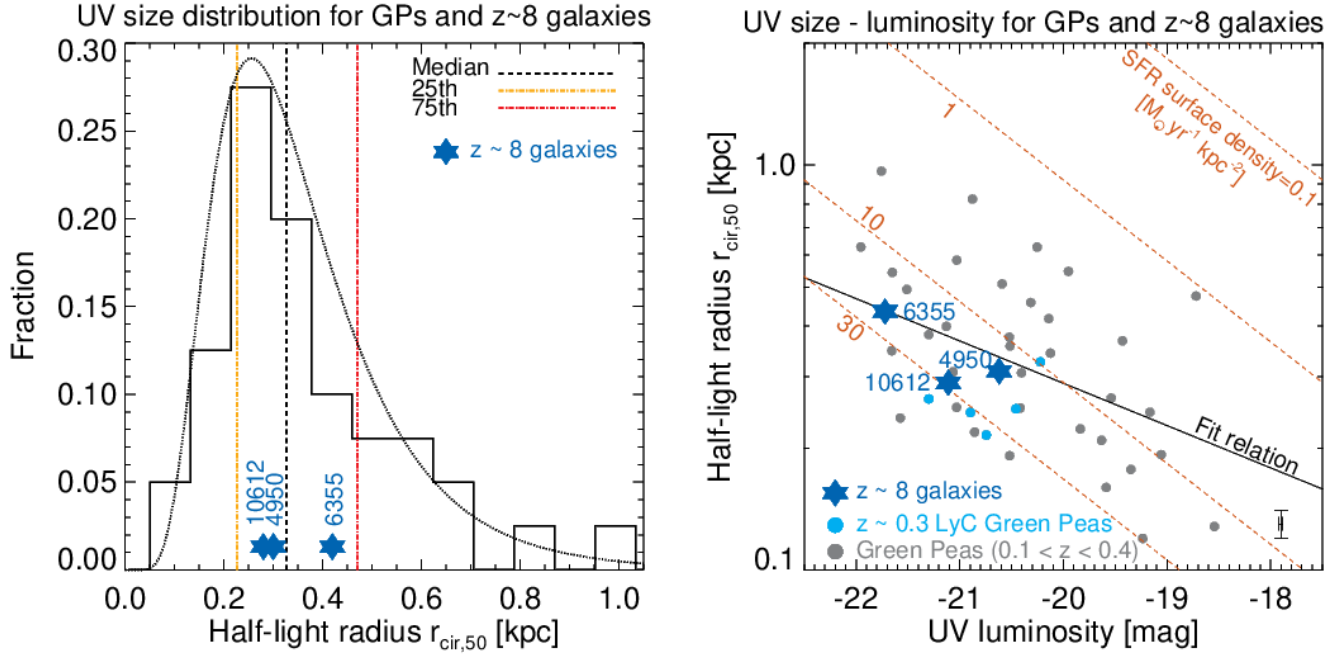


Figure 6. Blue star-shaped symbols mark the sizes and magnitudes of the *JWST* $z \sim 8$ galaxies compared to local analogs. Left: Histogram of Green Pea sizes (based on Kim et al. (2021)). All three *JWST* sources lie in the 2nd or 3rd quartile of Green Pea sizes. Right: Absolute magnitude vs. size, with contours of constant star formation intensity (i.e., orange dashed lines) marked. **Gray symbols** mark Green Peas. Pale blue symbols mark known Lyman continuum leaders (Izotov et al. 2016). The *JWST* sources populate the region of parameter space with the highest star formation intensity, which is also the region where known Lyman continuum leaders occur.

at considerably lower temperatures (fig. 4; and Netzer 1990; Osterbrock & Ferland 2006). While the observed ratio $f(\text{[O II]}\lambda 3729)/f(\text{[O II]}\lambda 3726)$ does not suggest such high densities, it is difficult to measure confidently given the resolving power of these spectra and the faintness of the $\text{[O II]}\lambda 3726, 3729$ lines; and moreover it is possible that $\text{[O III]}\lambda 4959, 5007$ emission takes place in denser regions of the galaxy than $\text{[O II]}\lambda 3726, 3729$ emission. Deeper $\text{[O II]}\lambda 3726, 3729$ spectra at NIRSpc’s highest resolution, or $\text{[S II]}\lambda 6716, 6731$ measurements using *JWST* MIRI spectroscopy, could shed further light on this.

An independent analysis of the line emission in these same galaxies and comparison to nearby analogs was recently published by Schaerer et al. (2022). While both their work and ours conclude that the *JWST* sources are of low metal abundance and are broadly similar to nearby analogs, there are substantial differences in some of our methodologies. In particular, they have applied a multiplicative correction (a power law of wavelength) to the spectra to bring the observed Balmer and oxygen line ratios into better agreement with theory, while we have analyzed those line ratios and concluded that within the uncertainties, no correction is required. As a result, we find a more extreme ratio of $\text{[O III]}\lambda 4363$ to $\text{[O III]}\lambda 4959, 5007$, and consequently a somewhat lower metal abundance in J072326-732656 (04590).

We now return to the larger question of how closely epoch-of-reionization galaxies resemble their best local analogs. We have shown clear resemblances in their emission-line-dominated rest-frame optical spectra (fig. 1) and in their small sizes and high surface brightnesses (fig. 6). The strong emission lines in both sets of galaxies suggest that their luminosities are strongly dominated by young stellar populations, and indeed the hydrogen line equivalent widths in Green Peas require substantial star formation within the last ~ 5 Myr.

On the other hand, low-redshift galaxies almost invariably show underlying, older stellar populations (age > 1 Gyr) when observed in sufficient detail to detect such populations in the presence of younger, brighter stars. Those underlying populations cannot be present in a universe that is only 0.7 Gyr old. Similarly, detailed abundance ratios in cosmic dawn galaxies may differ from those in older objects, given that entire classes of star may not have had the time to return products of their nuclear burning to the interstellar medium. Such abundance ratio differences may have an impact on the composition of interstellar dust in these early galaxies. It may be possible to probe gas-phase abundance

ratios in some detail with future *JWST* NIRSpec and MIRI spectroscopy. Stellar continuum absorption features may be within reach in a few more years, using 30-meter class telescopes.

We anticipate another important similarity between these galaxies and their local analogs: The likely presence of strong Ly α emission. Among Green Peas, strong Ly α is nearly ubiquitous (Henry et al. 2015; Yang et al. 2016, 2017). While the present *JWST* spectra do not cover Ly α for these sources, earlier surveys have found Ly α emitting galaxies up to these same redshifts, based on Lyman break selection (Oesch et al. 2015; Zitrin et al. 2015), narrowband imaging (the DAWN survey; Tilvi et al. 2020), or direct slitless spectroscopy (the FIGS survey, Tilvi et al. 2016; Larson et al. 2018). And identification of probable Ly α emitters has been demonstrated not only at low- z (Henry et al. 2015; Yang et al. 2016) but also in the epoch of reionization using Spitzer photometry to identify the strongest [O III]4959,5007 emitters (Roberts-Borsani et al. 2016). The statistics of Ly α emission among these early galaxies will be a valuable probe of reionization history (Malhotra & Rhoads 2004). In particular, if Ly α is detected in these objects, it will be possible to measure the Ly α escape fraction by comparison with the Balmer H β line, and to estimate what part of Ly α attenuation is due to the intergalactic medium and what part intrinsic to the galaxy using the Yang relation between velocity offset, dust reddening, and Ly α escape (Yang et al. 2017).

Finally, these *JWST* galaxies are likely giving us our first detailed look at the sources driving cosmological reionization. Green Peas include a high fraction of galaxies with substantial Lyman continuum escape (Izotov et al. 2016, 2018). The observable properties of these *JWST* targets closely resemble those of Green Peas. Beyond the spectroscopic similarity (fig. 1), their star formation intensities rank among the highest seen in the Green Pea sample, in a region of parameter space inhabited by the strongest known Lyman continuum leakers among the Green Peas (figure 6).

5. CONCLUSIONS

We have analyzed the rest-frame optical spectra of three epoch-of-reionization galaxies from the *JWST* Early Release Observations on the SMACS 0723 field. These objects are all strong line emitters, with spectra reminiscent of nearby Green Pea galaxies, and also of narrowband-selected extreme emission line galaxies at intermediate redshifts. This result supports earlier conclusions that Green Peas are among the best nearby analogs to high redshift galaxies.

The highest redshift and most extreme among these galaxies, J072326-732656 (04590) at $z = 8.495$, has a very low gas phase metallicity, $12 + \log[\text{O}/\text{H}] \approx 6.9 \pm 0.15$ from the T_e method, and $12 + \log[\text{O}/\text{H}] \approx 7.1$ from the Jiang et al. (2019) calibration of the strong line R₂₃ method. Its [O III]4363/[O III]4959,5007 ratio may demand the presence of a heating mechanism beyond photoheating by a young starburst. The other two galaxies, J072322-732606 (06355) at $z = 7.664$ and J072320-732604 (10612) at $z = 7.659$ have appreciably higher metallicities, in the range $7.7 < 12 + \log[\text{O}/\text{H}] < 8.2$. They demonstrate empirically that galaxy formation and stellar nucleosynthesis can achieve a metal abundance comparable to the Magellanic Clouds Russell & Dopita (1992) within just 700 Myr after the Big Bang.

All three of these galaxies share the compact sizes and high surface brightnesses that characterize Ly α emitting galaxies across a wide range of redshifts, from $z \sim 6.5$ down to $z \sim 0$ (Malhotra et al. 2012; Kim et al. 2020, 2021).

Low-redshift analogs for epoch-of-reionization galaxies have been of tremendous value in recent years, because they allowed us to study in nearby objects properties that could not be directly studied in faint, redshifted galaxies at Cosmic Dawn. As we have demonstrated, *JWST* now enables direct measurements of the many physically interesting quantities that can be derived from rest-frame optical emission lines. These will ultimately include metallicity, temperature, ionization parameter, density, and gas pressure. Despite this, the importance of local analogs remains. Some properties remain beyond reach at high redshift due to sensitivity. For example, radio emission from atomic gas in single galaxies can be studied in green peas (Kanekar et al. 2021; Purkayastha et al. 2022) but is far beyond reach in the early universe. Other important measurements are more fundamentally precluded at high redshift, notably including the escape fraction of ionizing radiation, which cannot be effectively observed at $z \gtrsim 4$ due to absorption by residual neutral gas in the intergalactic medium. The detection of Lyman continuum escape fractions of tens of percent, and even $> 50\%$ in some Green Pea galaxies, is a key ingredient in understanding reionization sources (Izotov et al. 2018; Flury et al. 2022a,b). Thus, *JWST* now equips us to establish the validity of local analog populations with unprecedented detail and confidence, opening the way for further progress using both the most distant and the closest young galaxies.

1 We thank the *JWST* team— *all* of you— for making this possible.

2 This work is based in part on observations made with the NASA/ESA/CSA James Webb Space Telescope. The
3 data were obtained from the Mikulski Archive for Space Telescopes at the Space Telescope Science Institute, which is
4 operated by the Association of Universities for Research in Astronomy, Inc., under NASA contract NAS 5-03127 for
5 JWST. These observations are associated with program #2736. The authors acknowledge the JWST ERO team for
6 developing their observing program with a zero-exclusive-access period.

7 This work has made use of public data from the Sloan Digital Sky Survey (SDSS). Funding for the SDSS and
8 SDSS-II has been provided by the Alfred P. Sloan Foundation, the Participating Institutions, the National Science
9 Foundation, the U.S. Department of Energy, the National Aeronautics and Space Administration, the Japanese Mon-
10 buka-gakusho, the Max Planck Society, and the Higher Education Funding Council for England. The SDSS Web Site
11 is <http://www.sdss.org/>.

12 The SDSS is managed by the Astrophysical Research Consortium for the Participating Institutions. The Participat-
13 ing Institutions are the American Museum of Natural History, Astrophysical Institute Potsdam, University of Basel,
14 University of Cambridge, Case Western Reserve University, University of Chicago, Drexel University, Fermilab, the
15 Institute for Advanced Study, the Japan Participation Group, Johns Hopkins University, the Joint Institute for Nuclear
16 Astrophysics, the Kavli Institute for Particle Astrophysics and Cosmology, the Korean Scientist Group, the Chinese
17 Academy of Sciences (LAMOST), Los Alamos National Laboratory, the Max-Planck-Institute for Astronomy (MPIA),
18 the Max-Planck-Institute for Astrophysics (MPA), New Mexico State University, Ohio State University, University of
19 Pittsburgh, University of Portsmouth, Princeton University, the United States Naval Observatory, and the University
20 of Washington.

REFERENCES

- Adams, N. J., Conselice, C. J., Ferreira, L., et al. 2022,
arXiv e-prints, arXiv:2207.11217.
<https://arxiv.org/abs/2207.11217>
- Alam, S., Albareti, F. D., Allende Prieto, C., et al. 2015,
ApJS, 219, 12, doi: [10.1088/0067-0049/219/1/12](https://doi.org/10.1088/0067-0049/219/1/12)
- Bertin, E., & Arnouts, S. 1996, A&AS, 117, 393,
doi: [10.1051/aas:1996164](https://doi.org/10.1051/aas:1996164)
- Bessell, M. S., Castelli, F., & Plez, B. 1998, A&A, 333, 231
- Bouwens, R. J., Illingworth, G. D., Oesch, P. A., et al.
2015, ApJ, 811, 140, doi: [10.1088/0004-637X/811/2/140](https://doi.org/10.1088/0004-637X/811/2/140)
- Brunker, S. W., Salzer, J. J., Janowiecki, S., Finn, R. A., &
Helou, G. 2020, ApJ, 898, 68,
doi: [10.3847/1538-4357/ab9ec0](https://doi.org/10.3847/1538-4357/ab9ec0)
- Byler, N., Kewley, L. J., Rigby, J. R., et al. 2020, ApJ, 893,
1, doi: [10.3847/1538-4357/ab7ea9](https://doi.org/10.3847/1538-4357/ab7ea9)
- Cardamone, C., Schawinski, K., Sarzi, M., et al. 2009,
MNRAS, 399, 1191,
doi: [10.1111/j.1365-2966.2009.15383.x](https://doi.org/10.1111/j.1365-2966.2009.15383.x)
- Carnall, A. C., Begley, R., McLeod, D. J., et al. 2022,
arXiv e-prints, arXiv:2207.08778.
<https://arxiv.org/abs/2207.08778>
- Castellano, M., Dayal, P., Pentericci, L., et al. 2016, ApJL,
818, L3, doi: [10.3847/2041-8205/818/1/L3](https://doi.org/10.3847/2041-8205/818/1/L3)
- Coe, D., Salmon, B., Bradač, M., et al. 2019, ApJ, 884, 85,
doi: [10.3847/1538-4357/ab412b](https://doi.org/10.3847/1538-4357/ab412b)
- Dimitrijević, M. S., Popović, L. Č., Kovačević, J., Dačić,
M., & Ilić, D. 2007, MNRAS, 374, 1181,
doi: [10.1111/j.1365-2966.2006.11238.x](https://doi.org/10.1111/j.1365-2966.2006.11238.x)
- Fan, X., Strauss, M. A., Becker, R. H., et al. 2006, AJ, 132,
117, doi: [10.1086/504836](https://doi.org/10.1086/504836)
- Ferland, G. J., Chatzikos, M., Guzmán, F., et al. 2017,
RMxAA, 53, 385. <https://arxiv.org/abs/1705.10877>
- Finkelstein, S. L., D’Aloisio, A., Paardekooper, J.-P., et al.
2019, ApJ, 879, 36, doi: [10.3847/1538-4357/ab1ea8](https://doi.org/10.3847/1538-4357/ab1ea8)
- Flury, S. R., Jaskot, A. E., Ferguson, H. C., et al. 2022a,
ApJS, 260, 1, doi: [10.3847/1538-4365/ac5331](https://doi.org/10.3847/1538-4365/ac5331)
- . 2022b, ApJ, 930, 126, doi: [10.3847/1538-4357/ac61e4](https://doi.org/10.3847/1538-4357/ac61e4)
- Goto, H., Shimasaku, K., Yamanaka, S., et al. 2021, ApJ,
923, 229, doi: [10.3847/1538-4357/ac308b](https://doi.org/10.3847/1538-4357/ac308b)
- Hathi, N. P., Malhotra, S., & Rhoads, J. E. 2008, ApJ, 673,
686, doi: [10.1086/524836](https://doi.org/10.1086/524836)
- Henry, A., Scarlata, C., Martin, C. L., & Erb, D. 2015,
ApJ, 809, 19, doi: [10.1088/0004-637X/809/1/19](https://doi.org/10.1088/0004-637X/809/1/19)
- Hu, W., Wang, J., Zheng, Z.-Y., et al. 2019, ApJ, 886, 90,
doi: [10.3847/1538-4357/ab4cf4](https://doi.org/10.3847/1538-4357/ab4cf4)
- Hu, W., Wang, J., Infante, L., et al. 2021, Nature
Astronomy, 5, 485, doi: [10.1038/s41550-020-01291-y](https://doi.org/10.1038/s41550-020-01291-y)
- Itoh, R., Ouchi, M., Zhang, H., et al. 2018, ApJ, 867, 46,
doi: [10.3847/1538-4357/aadfe4](https://doi.org/10.3847/1538-4357/aadfe4)
- Izotov, Y. I., Schaerer, D., Thuan, T. X., et al. 2016,
MNRAS, 461, 3683, doi: [10.1093/mnras/stw1205](https://doi.org/10.1093/mnras/stw1205)

- Izotov, Y. I., Stasińska, G., Meynet, G., Guseva, N. G., & Thuan, T. X. 2006, *A&A*, 448, 955, doi: [10.1051/0004-6361:20053763](https://doi.org/10.1051/0004-6361:20053763)
- Izotov, Y. I., Worseck, G., Schaerer, D., et al. 2018, *MNRAS*, 478, 4851, doi: [10.1093/mnras/sty1378](https://doi.org/10.1093/mnras/sty1378)
- Jaskot, A. E., & Oey, M. S. 2013, *ApJ*, 766, 91, doi: [10.1088/0004-637X/766/2/91](https://doi.org/10.1088/0004-637X/766/2/91)
- Jiang, T., Malhotra, S., Rhoads, J. E., & Yang, H. 2019, *ApJ*, 872, 145, doi: [10.3847/1538-4357/aeee8a](https://doi.org/10.3847/1538-4357/aeee8a)
- Kakazu, Y., Cowie, L. L., & Hu, E. M. 2007, *ApJ*, 668, 853, doi: [10.1086/521333](https://doi.org/10.1086/521333)
- Kanekar, N., Ghosh, T., Rhoads, J., et al. 2021, *ApJL*, 913, L15, doi: [10.3847/2041-8213/abfb76](https://doi.org/10.3847/2041-8213/abfb76)
- Kim, K., Malhotra, S., Rhoads, J. E., Butler, N. R., & Yang, H. 2020, *ApJ*, 893, 134, doi: [10.3847/1538-4357/ab7895](https://doi.org/10.3847/1538-4357/ab7895)
- Kim, K. J., Malhotra, S., Rhoads, J. E., & Yang, H. 2021, *ApJ*, 914, 2, doi: [10.3847/1538-4357/abf833](https://doi.org/10.3847/1538-4357/abf833)
- Larson, R. L., Finkelstein, S. L., Pirzkal, N., et al. 2018, *ApJ*, 858, 94, doi: [10.3847/1538-4357/aab893](https://doi.org/10.3847/1538-4357/aab893)
- Ly, C., Malhotra, S., Malkan, M. A., et al. 2016, *ApJS*, 226, 5, doi: [10.3847/0067-0049/226/1/5](https://doi.org/10.3847/0067-0049/226/1/5)
- Malhotra, S., & Rhoads, J. E. 2004, *ApJL*, 617, L5, doi: [10.1086/427182](https://doi.org/10.1086/427182)
- Malhotra, S., Rhoads, J. E., Finkelstein, S. L., et al. 2012, *ApJL*, 750, L36, doi: [10.1088/2041-8205/750/2/L36](https://doi.org/10.1088/2041-8205/750/2/L36)
- Meurer, G. R., Heckman, T. M., Lehnert, M. D., Leitherer, C., & Lowenthal, J. 1997, *AJ*, 114, 54, doi: [10.1086/118452](https://doi.org/10.1086/118452)
- Miralda-Escude, J., & Rees, M. J. 1998, *ApJ*, 497, 21, doi: [10.1086/305458](https://doi.org/10.1086/305458)
- Morisset, C. 2013, pyCloudy: Tools to manage astronomical Cloudy photoionization code, Astrophysics Source Code Library, record ascl:1304.020. <http://ascl.net/1304.020>
- Naidu, R. P., Tacchella, S., Mason, C. A., et al. 2020, *ApJ*, 892, 109, doi: [10.3847/1538-4357/ab7cc9](https://doi.org/10.3847/1538-4357/ab7cc9)
- Netzer, H. 1990, in *Active Galactic Nuclei*, ed. R. D. Blandford, H. Netzer, L. Woltjer, T. J. L. Courvoisier, & M. Mayor, 57–160
- Oesch, P. A., van Dokkum, P. G., Illingworth, G. D., et al. 2015, *ApJL*, 804, L30, doi: [10.1088/2041-8205/804/2/L30](https://doi.org/10.1088/2041-8205/804/2/L30)
- Osterbrock, D. E., & Ferland, G. J. 2006, *Astrophysics of gaseous nebulae and active galactic nuclei* (Sausalito, California: University Science Books)
- Planck Collaboration, Adam, R., Ade, P. A. R., et al. 2016, *A&A*, 594, A1, doi: [10.1051/0004-6361/201527101](https://doi.org/10.1051/0004-6361/201527101)
- Purkayastha, S., Kanekar, N., Chengalur, J. N., et al. 2022, *ApJL*, 933, L11, doi: [10.3847/2041-8213/ac7522](https://doi.org/10.3847/2041-8213/ac7522)
- Rigby, J., Perrin, M., McElwain, M., et al. 2022, arXiv e-prints, arXiv:2207.05632. <https://arxiv.org/abs/2207.05632>
- Roberts-Borsani, G. W., Bouwens, R. J., Oesch, P. A., et al. 2016, *ApJ*, 823, 143, doi: [10.3847/0004-637X/823/2/143](https://doi.org/10.3847/0004-637X/823/2/143)
- Robertson, B. E., Ellis, R. S., Furlanetto, S. R., & Dunlop, J. S. 2015, *ApJL*, 802, L19, doi: [10.1088/2041-8205/802/2/L19](https://doi.org/10.1088/2041-8205/802/2/L19)
- Russell, S. C., & Dopita, M. A. 1992, *ApJ*, 384, 508, doi: [10.1086/170893](https://doi.org/10.1086/170893)
- Sanders, R. L., Shapley, A. E., Kriek, M., et al. 2016, *ApJ*, 816, 23, doi: [10.3847/0004-637X/816/1/23](https://doi.org/10.3847/0004-637X/816/1/23)
- Schaerer, D., Marques-Chaves, R., Oesch, P., et al. 2022, arXiv e-prints, arXiv:2207.10034. <https://arxiv.org/abs/2207.10034>
- Stark, D. P., Ellis, R. S., Chiu, K., Ouchi, M., & Bunker, A. 2010, *MNRAS*, 408, 1628, doi: [10.1111/j.1365-2966.2010.17227.x](https://doi.org/10.1111/j.1365-2966.2010.17227.x)
- Stasińska, G. 1990, *A&AS*, 83, 501
- Steidel, C. C., Rudie, G. C., Strom, A. L., et al. 2014, *ApJ*, 795, 165, doi: [10.1088/0004-637X/795/2/165](https://doi.org/10.1088/0004-637X/795/2/165)
- Tilvi, V., Pirzkal, N., Malhotra, S., et al. 2016, *ApJL*, 827, L14, doi: [10.3847/2041-8205/827/1/L14](https://doi.org/10.3847/2041-8205/827/1/L14)
- Tilvi, V., Malhotra, S., Rhoads, J. E., et al. 2020, *ApJL*, 891, L10, doi: [10.3847/2041-8213/ab75ec](https://doi.org/10.3847/2041-8213/ab75ec)
- Wold, I. G. B., Malhotra, S., Rhoads, J., et al. 2022, *ApJ*, 927, 36, doi: [10.3847/1538-4357/ac4997](https://doi.org/10.3847/1538-4357/ac4997)
- Yang, H., Malhotra, S., Gronke, M., et al. 2016, *ApJ*, 820, 130, doi: [10.3847/0004-637X/820/2/130](https://doi.org/10.3847/0004-637X/820/2/130)
- . 2017, *ApJ*, 844, 171, doi: [10.3847/1538-4357/aa7d4d](https://doi.org/10.3847/1538-4357/aa7d4d)
- Yang, H., Infante, L., Rhoads, J. E., et al. 2019, *ApJ*, 876, 123, doi: [10.3847/1538-4357/ab16ce](https://doi.org/10.3847/1538-4357/ab16ce)
- Yang, J., Wang, F., Fan, X., et al. 2020, *ApJL*, 897, L14, doi: [10.3847/2041-8213/ab9c26](https://doi.org/10.3847/2041-8213/ab9c26)
- Zheng, Z.-Y., Wang, J., Rhoads, J., et al. 2017, *ApJL*, 842, L22, doi: [10.3847/2041-8213/aa794f](https://doi.org/10.3847/2041-8213/aa794f)
- Zitrin, A., Labbé, I., Belli, S., et al. 2015, *ApJL*, 810, L12, doi: [10.1088/2041-8205/810/1/L12](https://doi.org/10.1088/2041-8205/810/1/L12)